LETTER • OPEN ACCESS

Top-down approach using supercritical carbon dioxide ball milling for producing sub-10 nm Bi_2Te_3 grains

View the article online for updates and enhancements.

LETTER

Top-down approach using supercritical carbon dioxide ball milling for producing sub-10 nm Bi_2Te_3 grains

Mohamed Atwa[1*] , Tessui Nakagawa[2], Akira Yonamine[3], David C. Lloyd[1], Makoto Schreiber[1], Koji Miyazaki[3,4], Tsunehiro Takeuchi[4,5], and Yoshinori Okada[1,5]

[1]Okinawa Institute of Science and Technology Graduate University, 1919-1, Tancha, Onna-son, Okinawa, 904-0412, Japan
[2]University of the Ryuukyus, Department of Chemistry, Nishihara-cho, Okinawa, 903-0213, Japan
[3]Kyuushu Institute of Technology, Department of Mechanical and Control Engineering, 1-1 Sensui-cho, Tobata-ku, Kitakyushu, Fukuoka, 804-8550, Japan
[4]CREST, Japan Science and Technology Agency, Tokyo, 102-0076, Japan
[5]Toyota Technological Institute, Nagoya, 468-8511, Japan

*E-mail: mohamed.atwa@oist.jp

We compare Bi_2Te_3 powders prepared by conventional ball milling to powders milled in supercritical carbon dioxide ($scCO_2$). We demonstrate that $scCO_2$ milling overcomes size-reduction limitations reported for conventional milling. XRD and TEM reveal nanograins with smaller average sizes (< 10 nm) and narrower grain size distributions in the $scCO_2$ milled case. $scCO_2$ milling also preserves the crystallinity and shows less oxidation than conventional milling. This is the first report of Bi_2Te_3 with a sub-10 nm grain size whilst conserving high quality crystallinity, made using a top-down approach. Our study offers a route for developing unprecedentedly fine bulk nanostructured Bi_2Te_3-based thermoelectric materials. © 2020 The Japan Society of Applied Physics

Supplementary material for this article is available online

Bi$_2$Te$_3$ is one of the most well-known and extensively studied thermoelectric materials, and its further functional improvement is believed to be possible via nanostructuring.[1] For example, numerous calculations have reported that 60%–80% of the cumulative lattice thermal conductivity (K_c) in Bi_2Te_3 can be attributed to phonons with a mean free path of less than 10 nm.[2,3] Although numerous bottom-up methods have already achieved sub-10 nm grain sizes and film thicknesses,[4–6] top-down size minimization methods are usually preferred for practical nanostructuring applications. This is because top-down methods are typically faster, higher yield, and more cost effective as compared to their bottom-up counterparts.[7] Several studies have reported on top-down approaches for nanostructuring Bi_2Te_3-based thermoelectric materials, including arc melting,[8] cryogenic grinding[9] bead milling,[10] and conventional ball milling.[11] However, none of these methods report average sizes of the resulting grains below 10 nm. The realization of sub-10 nm mean sizes in bulk nanostructured Bi_2Te_3 would lead to unprecedented enhancements in the thermoelectric figure of merit, zT in practical devices.[1]

Among the existing top-down techniques employed in Bi_2Te_3 nanostructuring, ball milling is by far the most popular,[11,12] owing to its high yield, cost-effectiveness, and scalability. However, an anomalous grain refinement effect limits the minimum achievable size of Bi_2Te_3 nanoparticles through conventional ball milling.[13] This is due to an eventual equilibrium between defect accumulation and adiabatic heating-induced recovery of defects with increasing milling time, which leads to steady state minimum sizes of around 20–50 nm.[13,14]

Bi_2Te_3 is a van der Waals (vDW) material that forms in a trigonal, layered structure consisting of Te–Bi–Te–Bi–Te quintuples with weakly coupled vDW gaps between the terminating Te layers.[15] Supercritical fluids can effectively intercalate the vDW gaps of layered materials due to their unique physiochemical properties; namely, they have densities comparable to liquids and zero surface tension, like gases.[16–18] Numerous studies have been conducted to date on the effective exfoliation of grapheme,[19] MoS_2[20,21] and hBN[22] using supercritical fluids. Among the supercritical fluids used for the exfoliation of vDW materials, $scCO_2$ is especially popular, owing to its readily accessible critical point (31 °C, 7.4 MPa), cheapness, abundance, nontoxicity, nonflammability, and relative environmental friendliness.[17] Reports have also remarked on the inertness of Bi_2Te_3 to reaction with CO_2, even in extreme conditions (460 °C/9.5 MPa).[23,24] To date, however, no studies have been conducted on the exfoliation of Bi_2Te_3 in $scCO_2$.

Using a synergistic combination of mechanical ball milling and $scCO_2$ exfoliation, we demonstrate that $scCO_2$ milling can overcome the size reduction limitations of conventional ball milling in Bi_2Te_3-based materials. To our knowledge, this is the first report of successful top-down nanostructuring of Bi_2Te_3 powders with sub-10 nm average sizes.

A description of the ball milling procedure used herein is presented schematically in Fig. 1(a). Bi_2Te_3 powders with a 50–100 μm starting particle size (Kojundo Chemical Laboratory Co. LTD.) were weighed and loaded with zirconia balls into custom-made high-pressure ball milling jars. Milling was done using Seiwa Giken RM-05 rocking mill with two jars as is common for mechanical ball milling. The ball milling procedure for the $scCO_2$ samples is depicted in Fig. 1(b). To simplify the experiments and capture the uniqueness of milling in $scCO_2$, one jar was designated for milling in $scCO_2$ and the other jar for milling in low pressure (LP) (0.1 MPa) CO_2. The conventionally milled samples, hereafter referred to as LP samples, were milled similarly, except the sealed jar was simply evacuated and filled with 0.1 MPa of CO_2 for a single run of milling. In this study, the
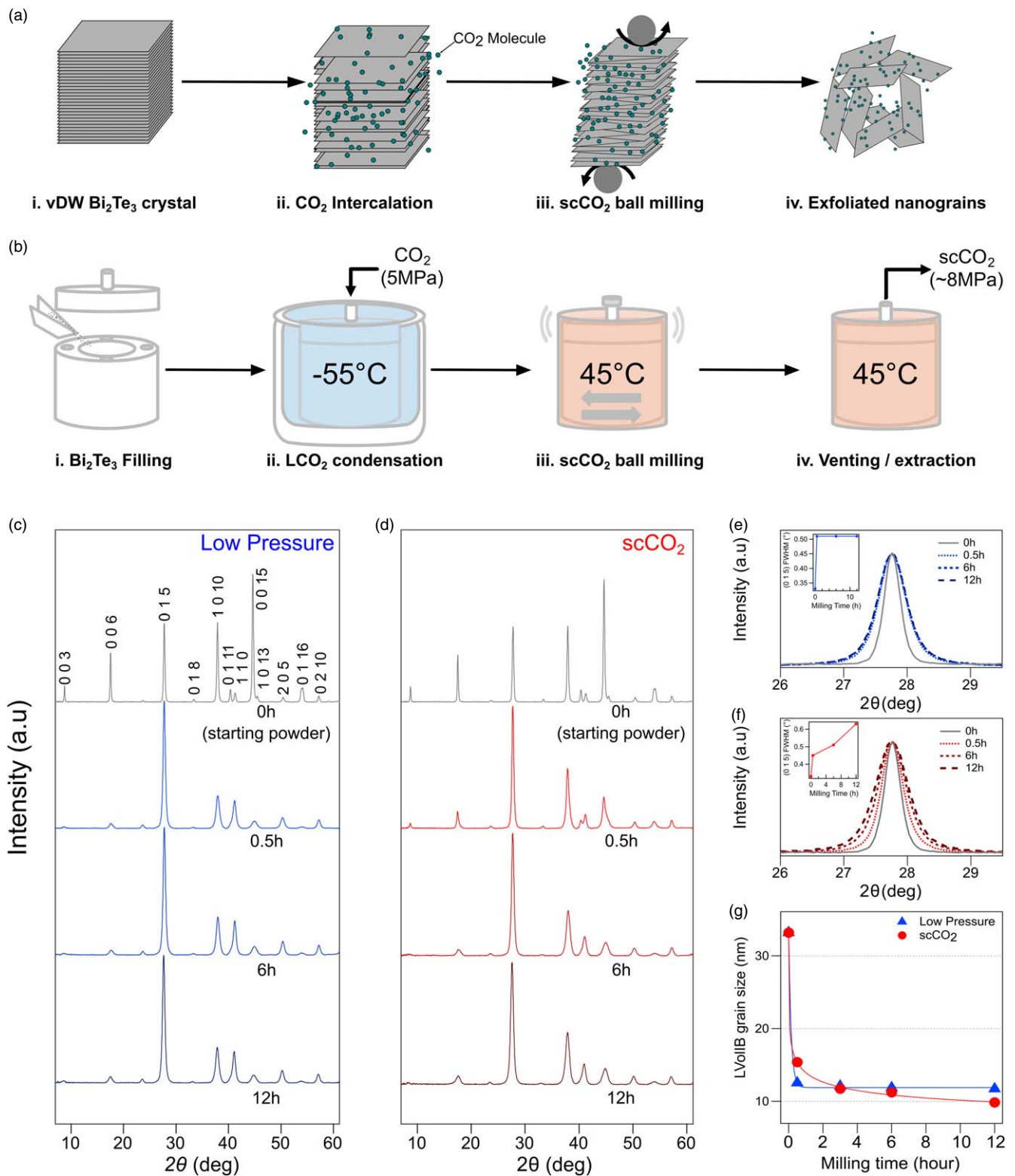
Fig. 1. (Color online) Ball milling and XRD peak analysis of the LP versus scCO$_2$ powders. (a) The size minimization schematic during scCO$_2$ ball milling. (b) Depiction of the scCO$_2$ ball milling procedure. (c) and (d) PXRD pattern survey of the LP and scCO$_2$ milling cases, respectively. (e) and (f) Normalized (0 1 5) peak of the LP and scCO$_2$ milling cases, respectively. (g) The average grain sizes of the LP and scCO$_2$ milling versus milling from peak-fitting. The average grain sizes of the powders were estimated from the pattern fittings using the LVol-IB method, under the assumption of isotropic size and strain using a Scherrer factor ($K = 0.89$).

LP and scCO$_2$ samples were milled for durations of 0.5, 3, 6, and 12 h. To minimize sample exposure to air, the starting Bi$_2$Te$_3$ powder was stored in an Ar glovebox. Additionally, filling and emptying the jars of powder were always conducted in an Ar glovebox. Additional milling parameters can be found in supplement S1, available online at stacks.iop. org/APEX/13/067002/mmedia.

To understand the difference in crystallinity and morphology between the LP and scCO$_2$ milling cases, we conducted powder X-ray diffraction (XRD). XRD characterization showed a clear difference in peak width between the
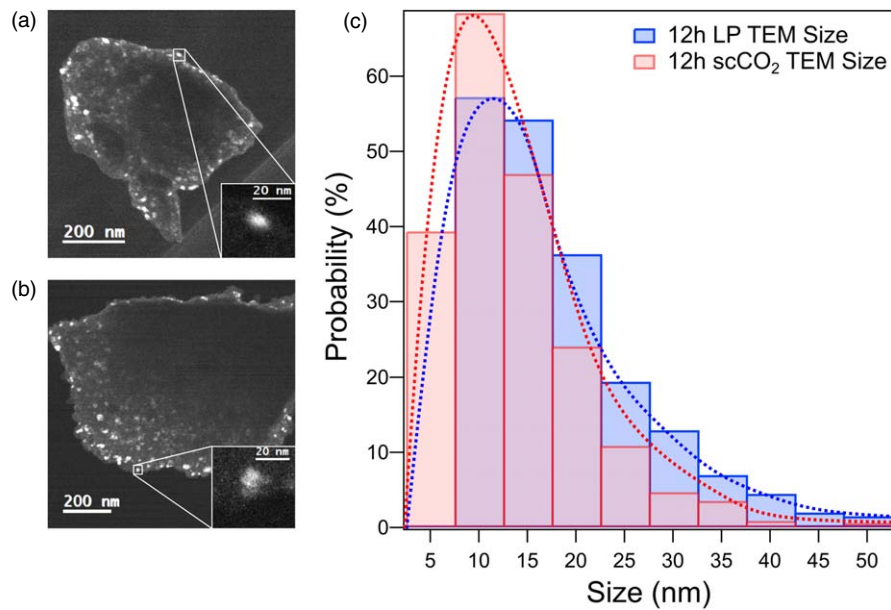
Fig. 2. (Color online) The dark field scanning transmission electron microscopy (DF-STEM) images and grain size distributions of the 12 h LP and scCO$_2$ cases obtained from the measurement of over 500 grains in both cases. (a) and (b) Typical DF-TEM image from the 12 h LP and scCO$_2$ milling cases respectively. Insets show typical grains measured to obtain the size distributions. (c) Normalized histograms of the grain size distributions with lognormal fittings in both the 12 h LP and 12 h scCO$_2$ cases.

LP and scCO$_2$ samples. In all XRD pattern acquisitions, the powders were loaded in the glove box into sealed cells designed to minimize powder exposure to air during XRD measurement. Figures 1(c) and 1(d) show the typical XRD patterns of the LP and scCO$_2$-milled samples. Both samples retain their crystallinity and are notably free of Bi$_2$Te$_3$–CO$_2$ reaction products or secondary off-stoichiometry Bi–Te phases, indicating the compatibility of scCO$_2$ as an inert supercritical fluid exfoliant for Bi$_2$Te$_3$. To measure XRD-peak broadening in each sample, the (015) peak was chosen for convenience, since it is well-disentangled from peaks of other indices. Figures 1(e) and 1(f) show the enlarged and normalized (015) peaks of both the LP and scCO$_2$ cases, respectively. A clear trend in peak broadening with increasing milling time was observed [inset of Figs. 2(c) and 2(d)]. This is an expected trend as the grain size of the powders is inversely proportional to XRD peak width based on the Scherrer equation $\beta = \frac{K\lambda}{L\cos(\theta)}$, which expresses the relationship between the grain size β and the peak breadth L, where K is the Scherrer factor, λ is the wavelength of the incident X-rays, and θ is the Bragg angle.

To confirm the difference in grain size evolution, multiple peaks were fitted in the 12°–51° 2θ range. As is typical for such fittings, the fundamental parameter approach was employed,[25] enabling the calculation of an averaged grain size and lattice strain from the XRD profile under the assumption of isotropic size and strain. The impact of preferential orientation for grain size estimation was minimized by putting a free parameter for this effect. The effect of strain on peak broadening is also accounted for and disentangled from the size broadening during the full pattern fittings, due to the difference in θ dependence of these two causes of peak broadening.[26] While peak broadening due to size exhibits a $\frac{1}{\cos(\theta)}$ dependence, strain broadening exhibits a $\tan(\theta)$ dependence. High quality fittings with weighted profile (R_{wp}) values <10 for all fittings[25] were achieved

for all XRD curves from different powders, as can be seen for a typical fitting in S2. The resultant time evolution of the grain sizes for the samples from scCO$_2$ and LP cases is shown in Fig. 1(g). The time dependence of strain is comparable between the LP and scCO$_2$ milling cases, as shown in S3. Both the LP and scCO$_2$ milling cases reach approximately 4.5% lattice strain after 12 h of ball milling. While the steady-state average grain size of the LP case saturates at ∼12 nm after 0.5 h milling, the scCO$_2$ average grain size reaches an estimated 9.83 nm in size after 12 h of milling. Moreover, the size reduction trend in the scCO$_2$ milled samples shows no sign of saturation, suggesting that even smaller average grain sizes may be achievable using this method. As presented in the following section, real space grain size variation has minimal impact on the size estimates obtained from XRD data.

In addition to the spatially-averaged grain size estimation from XRD, characterization of grain size variation using dark field transmission electron microscopy (DF-TEM) imaging further provides a consistent picture of the nanoscale morphology. DF-TEM provides images of high contrast sensitive to crystal structure while removing contributions from the mass-thickness contrast that bright field TEM imaging is susceptible to. Together, these factors make DF-TEM useful for determining the grain size distribution in real space with high statistics.[27] Figures 2(a) and 2(b) show DF-TEM images from the 12 h LP and 12 h scCO$_2$ cases, respectively. To determine the difference in grain size distribution between the LP and scCO$_2$ samples, the longest edge-to-edge length of every grain for ∼500 grains were measured to within one standard deviation from the mean value for each sample from the resulting DF-TEM images [Fig. 2(c)]. Notably, scCO$_2$ milling results in a significant fraction of grains with sizes between 0 and 5 nm while LP milling does not. This further confirms that scCO$_2$ milling is

capable of achieving smaller grain sizes inaccessible by LP milling.

Before showing the well-defined atomic structures in single grains of $scCO_2$-milled Bi_2Te_3, we point out the surprising advantage of reduced surface oxidation from $scCO_2$ milling. To probe this, X-ray photoemission spectroscopy (XPS) of the Bi 3d and Te 4f core levels are compared between. We focus on comparing the pristine powder (as received from the vendor), with the 6 h LP and $scCO_2$ milling cases, as the latter two exhibit similar grain size (and consequently similar surface/bulk ratio). Samples were taken out of the glovebox simultaneously and immediately loaded into an AXIS Ultra HSA XPS system for measurement. Figures 3(a) and 3(b) show the normalized Bi 3d/13 and Te 4f/14 core levels, respectively, of the 6 h LP and $scCO_2$ samples. The intensity of the Bi–O and Te–O oxygen peaks are clearly stronger in the 6 h LP case than in the 6 h $scCO_2$ case. Elemental ratios from quantitative analysis of the peak profiles are shown in Fig. 3(c). Despite having similar grain sizes, the Bi–O ratio of the 6 h $scCO_2$ case is about 44% lower than the LP case. Similarly, the Te–O ratio of the 6 h $scCO_2$ case is approximately 55% lower than the LP. These findings suggest that $scCO_2$ may passivate the surface of the Bi_2Te_3 and prevent additional oxidation. This highlights another benefit of $scCO_2$ milling in reducing the impact of detrimental surface oxidization previously reported for conventional milling cases.[28]

To investigate atomic arrangement of these individual non-oxidized grains, high-angle annular dark-field scanning transmission electron microscopy (HAADF-STEM) imaging was used. The HAADF-STEM technique provides Z-contrast at atomic resolution, revealing high quality local crystallinity within each grain and the existence of abrupt grain boundaries within the 10 nm length scale. Figures 4(a)–4(c) show HAADF-STEM images of powders from the 6 h $scCO_2$ milling case. Figure 4(a) highlights the well-defined out-of-
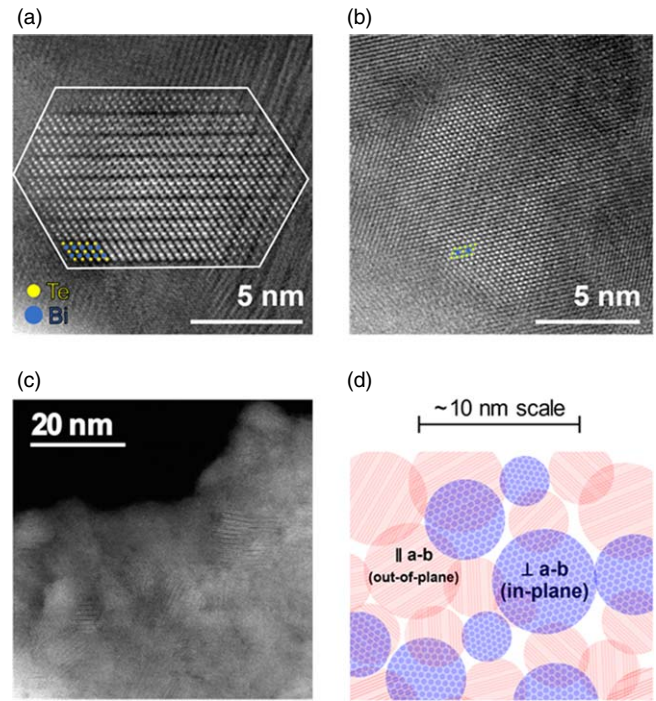
Fig. 4. (Color online) The high-angle annular dark field scanning transmission electron microscopy (HAADF-STEM) images of the 6 h $scCO_2$-milled sample. HAADF-STEM images of the out-of-plane (a) in-plane (b) and mixed grain-microstructure (c) of the 6 h $scCO_2$ milling case. (d) Schematic depiction of the resultant grain structure based on (c).

plane atomic arrangement within a single grain. The quintuple-layered features can be clearly observed. Similarly, Fig. 4(b) highlights the in-plane atomic arrangements within grains, where planar 6-fold symmetry can be observed. Both are expected features based on bulk crystal structure of Bi_2Te_3. Our atomic scale characterization supports that crystallinity is well-conserved within each grain, even down to the 10 nm scale. In addition to this local structure,

Sample	Bi-Te	Bi-O	Te-Bi	Te-O
Pristine	1.0	2.3	1.0	2.4
6h LP	1.0	0.9	1.0	0.9
6h scCO₂	1.0	**0.5**	1.0	**0.4**
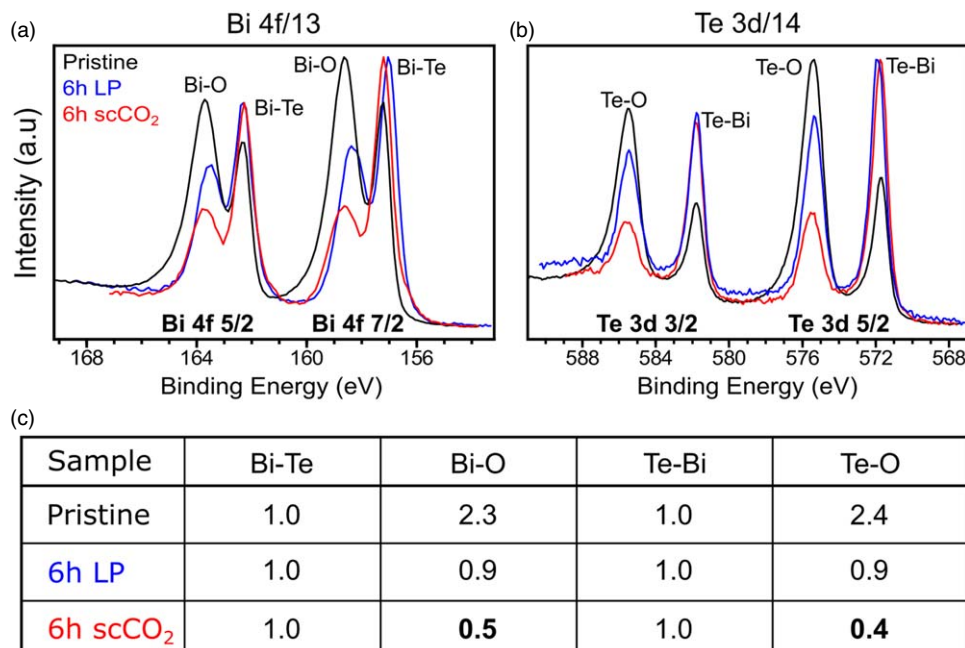
Fig. 3. (Color online) X-Ray photoemission spectroscopy of the pristine powder, the 6 h LP milled sample, and the 6 h $scCO_2$ milled sample. (a) and (b) Normalized Bi 3d/13 and Te 4f/14 core levels, respectively, of the pristine, 6 h LP and $scCO_2$ samples. (c) Elemental ratios from quantitative analysis of the peak profiles. The 6 h $scCO_2$ milling case exhibits the lowest degree of surface oxidation, when compared with the 6 h LP and pristine powders.

aspects of inter-grain connectivity are interesting in terms of phonon-blocking in Bi_2Te_3. Figure 4(c) shows a zoomed-out region where both the in-plane and out-of-plane oriented grains coexist and are interconnected, which is schematically drawn in Fig. 4(d). This rich, fine microstructure that results from $scCO_2$ milling could result in various unprecedent effects, which we now discuss.

Our powder with sub-10 nm grains will be a crucial starting material for the realization of bulk nanostructure Bi_2Te_3 with a high density of grain boundaries and various types of atomic interfaces with different crystalline orientations. The realization of rich atomic-scale grain boundaries within the $\sim$10 nm scale is an exciting future platform for phonon-blockage-based thermal management. This is because 80% of lattice thermal conductivity is expected to arise from phonons with a mean free path of less than 10 nm in Bi_2Te_3.[2,3] Furthermore, our method of making high quality sub-10 nm grains may provide a novel arena for the integration of exotic thermoelectric functionality driven by topologically protected helical Dirac states.[29] While such states have already been observed in epitaxial films of Bi_2Te_3, our method could be the starting point for introducing them into a functional macroscopic thermoelectric device. Our findings could also be expanded to the design of heterogeneous vdW systems for tailored p–n junctions, magnetic junctions, and topologically non-trivial edge states. Overall, we think that our findings may provide a new means to leverage interesting interfacial/grain dominated functionality in extended 3D networks of various vdW systems.

To our knowledge, we report on the first-ever achievement of Bi_2Te_3 nanoparticles with average sizes smaller than 10 nm using a top-down method, via milling in supercritical carbon dioxide. The milling of Bi_2Te_3 in supercritical carbon dioxide is shown to be conclusively superior to conventional milling, overcoming the minimum steady state saturation size reported for conventional ball milling.[13] XPS analysis shows that $scCO_2$ milling also results in a significantly lower degree of surface oxidation as compared to conventional milling. The realization of sub-10 nm scale grains is integral for the development of high-performance bulk nanostructured Bi_2Te_3-based thermoelectric materials. This study paves the way for the realization of Bi_2Te_3-based thermoelectrics with unprecedented phonon-blocking properties. Furthermore, the unique capabilities of $scCO_2$ provide universal advantages in producing various interesting nanostructured vdW materials.

Competing interests statement

The authors declare that they have no known competing financial interests or personal relationships that could have appeared to influence the work reported in this paper.

ORCID iDs   Mohamed Atwa https://orcid.org/0000-0001-5310-360X

1) L. D. Hicks and M. S. Dresselhaus, Phys. Rev. B **47**, 12727 (1992).
2) L. Bulat, D. Pshenay-Severin, V. Osvenskii, and Y. N. Parkhomenko, Semiconductors **51**, 695 (2017).
3) Y. Wang, B. Qiu, A. J. McGaughey, X. Ruan, and X. Xu, J. Heat Transf. **135**, 091102 (2013).
4) M. Kashiwagi, S. Hirata, K. Harada, Y. Zheng, K. Miyazaki, M. Yahiro, and C. Adachi, Appl. Phys. Lett. **98**, 023114 (2011).
5) L. Tuyen, P. Le, C. Luo, and J. Leu, J Alloys Compd. **673**, 107 (2016).
6) M. Takashiri, K. Hagiwara, and J. Hamada, Vacuum **157**, 216 (2018).
7) G. Tan, L.-D. Zhao, and M. G. Kanatzidis, Chem. Rev. **116**, 12123 (2016).
8) F. Serrano-Sánchez, M. Gharsallah, N. M. Nemes, N. Biskup, M. Varela, J. L. Martínez, M. T. Fernández-Díaz, and J. A. Alonso, Sci. Rep. **7**, 6277 (2017).
9) X. Chen, L. Liu, Y. Dong, L. Wang, L. Chen, and W. Jiang, Prog. Nat. Sci.: Mater. Int. **22**, 201 (2012).
10) M. Takashiri, S. Tanaka, M. Takiishi, M. Kihara, K. Miyazaki, and H. Tsukamoto, J Alloys Compd. **462**, 351 (2008).
11) B. Poudel et al., Science **320**, 634 (2008).
12) Y. Ma, Q. Hao, B. Poudel, Y. Lan, B. Yu, D. Wang, G. Chen, and Z. Ren, Nano Lett. **8**, 2580 (2008).
13) S. A. Humphry-Baker and C. A. Schuh, Acta Mater. **75**, 167 (2014).
14) Y. Lan, B. Poudel, Y. Ma, D. Wang, M. S. Dresselhaus, G. Chen, and Z. Ren, Nano Lett. **9**, 1419 (2009).
15) D. Teweldebrhan, V. Goyal, and A. A. Balandin, Nano Lett. **10**, 1209 (2010).
16) Y. Ren and Q. Xu, Energy Environ. Mater. **1**, 46 (2018).
17) Z. Sun, Q. Fan, M. Zhang, S. Liu, H. Tao, and J. Texter, Adv. Sci. **6**, 1901084 (2019).
18) J. Peach and J. Eastoe, Beilstein J. Org. Chem. **10**, 1878 (2014).
19) Y. Wang, Z. Chen, Z. Wu, Y. Li, W. Yang, and Y. Li, Langmuir **34**, 7797 (2018).
20) Y. Wang, C. Zhou, W. Wang, and Y. Zhao, Ind. Eng. Chem. Res. **52**, 4379 (2013).
21) Q. D. Truong, M. K. Devaraju, Y. Nakayasu, N. Tamura, Y. Sasaki, T. Tomai, and I. Honma, ACS Omega **2**, 2360 (2017).
22) X. Tian, Y. Li, Z. Chen, Q. Li, L. Hou, J. Wu, Y. Tang, and Y. Li, Sci. Rep. **7**, 17794 (2017).
23) S. T. Port, E. Kohler, and V. Chevrier, 48th Lunar and Planetary Science Conf., abs #1081, 2017.
24) E. Kohler, S. Port, V. Chevrier, N. Johnson, and C. Lacy, 46th Lunar and Planetary Science Conf., abs #2653, 2015.
25) B. H. Toby, Powder Diffr. **21**, 67 (2006).
26) R. L. Snyder, J. Fiala, H. J. Bunge, H. J. Bunge, and I. U. of Crystallography, *Defect and Microstructure Analysis by Diffraction* (Oxford University Press, Oxford, 1999).
27) W. D. Pyrz and D. J. Buttrey, Langmuir **24**, 11350 (2008).
28) J. Kim, L. T. Duy, B. Ahn, and H. Seo, J. Asian Ceram. Soc. **8**, 211 (2020).
29) H. Zhang, C.-X. Liu, X.-L. Qi, X. Dai, Z. Fang, and S.-C. Zhang, Nat. Phys. **5**, 438 (2009).